Effect of strain on low-loss electron energy loss spectra of group-III nitrides

J. Palisaitis,* C.-L. Hsiao, M. Junaid, J. Birch, L. Hultman, and P. O. Å. Persson

Thin Film Physics Division, Department of Physics, Chemistry, and Biology (IFM), Linköping University, SE-58183, Linköping, Sweden

(Received 17 May 2011; revised manuscript received 8 November 2011; published 7 December 2011)

Thin films of AlN experiencing different strain states were investigated with a scanning transmission electron microscope (STEM) by low-loss electron energy loss spectroscopy (EELS). The results conclude that the low-loss properties and in particular, the plasmon peak position is shifted as a direct consequence of the inherent strain of the sample. The results reveal that strain, even minor levels, can be measured by STEM-EELS. These results were further corroborated by full potential calculations and expanded to include the similar III nitrides GaN and InN. It is found that a unit-cell volume change of 1% results in a bulk plasmon peak shift of 0.159, 0.168, and 0.079 eV for AlN, GaN, and InN, respectively, according to simulations. The AlN peak shift was experimentally corroborated with a corresponding peak shift of 0.156 eV. The unit-cell volume is used here since it is found that regardless of in- and out-of-plane lattice augmentation, the low-loss properties appear near identical for constant volume. These results have an impact on the interpretation of the plasmon energy and its applicability for determining and separating stress and composition. It is found that while the bulk plasmon energy can be used as a measure of the composition in a group-III nitride alloy for relaxed structures, the presence of strain significantly affects such a measurement. The strain is found to have a lower impact on the peak shift for $Al_{1-x}In_xN$ (~3% compositional error per 1% volume change) and $In_{1-x}Ga_xN$ alloys compared to significant variations for $Al_{1-x}Ga_xN$ (16% compositional error for 1% volume change). Hence a key understanding in low-loss studies of III nitrides is that strain and composition are coupled and affect one another.

DOI: 10.1103/PhysRevB.84.245301 PACS number(s): 79.20.Uv, 71.45.Gm, 68.60.Bs, 81.05.Ea

I. INTRODUCTION

Group-III nitride semiconductor alloys attract interest due to promising applications for optoelectronic and electronic devices due to unique physical properties and engineering capabilities.[1] At the same time, modern electronic devices are increasingly employing structures which are dimensioned on the nanoscale,[2] such as optical devices based on quantum wells. As the structures are shrinking, the impact of strain, which appears when a material of a given structure, specific composition, and lattice parameters is adapting to a second material, has a significant impact on device characteristics. This is commonly used to increase performance, e.g., in strained SiGe layer devices.[3,4] Device performance is affected not only by strain in the active layers, but also by the composition of the layer. To achieve a thorough understanding of the device performance, one should seek to separate and identify the impact of both strain and compositional variations, even on the nanoscale. However, the composition affects the lattice parameter, which is also affected by strain. While strain and composition can commonly be measured by x-ray diffraction (XRD) or Raman spectroscopy, the two components are not easily separated. Decoupling of compositional and strain effects on the macroscopic level can be achieved by combining XRD with Rutherford backscattering spectroscopy (RBS).[5] However, for performing strain and compositional investigations on the nanometer scale (e.g., in an individual quantum well), a superior spatial resolution is required and can be achieved in the scanning transmission electron microscope (STEM).

Various methods have been employed in the STEM to obtain a measure of strain, such as the geometric phase analysis (GPA)[6] and peak pairs analysis (PPA).[7] Furthermore, strain has been investigated by convergent-beam electron diffraction (CBED)[8] and nanobeam electron diffraction (NBD),[9] as well as by nanoscale holographic interferometry.[10] The ability to separate the information into strain and composition on nanoscale proves to be challenging. As an example, GPA and PPA are based on evaluation of the crystal lattice spacing, which regretfully depends on both strain and composition. A successful approach to resolve strain and composition is to combine interferometry and GPA methods, where strain and composition can be measured with 2 nm resolution and with 0.1% and 5% accuracy in lattice strain and composition, respectively.[11]

Electron energy-loss spectroscopy (EELS) was not so extensively used for strain characterization. In the low-loss region of the energy-loss spectrum, the major features of the loss function are interband transitions and bulk plasmon losses. Bulk plasmon losses, to a first approximation, correspond to a collective oscillation of the valence electrons and the energy of this oscillation is given by the valence electron density of the material system.[12] Since the valence electron density is highly dependent on the material properties, such as strain and composition,[13] it becomes increasingly promising to pursue an increased understanding of electronic and optical properties of a material through a more careful investigation of the low-loss function,[14] for which initial attempts have been made.[15] It was thus shown that the bulk plasmon peak may be used to determine the composition in group-III nitride alloys, e.g., $Al_{1-x}In_xN$, from a linear shift of the plasmon energy in relaxed layers.[16] However, the effect of strain in combination with compositional variations on the bulk plasmon peak has not been thoroughly investigated, although a shift in peak position has been suggested.[15]

Recent improvements in microscopy[17] and spectroscopy instrumentaton[18] is paving the way for acquiring analytical images at nearly the same speed as was previously required to record plain STEM images. Now, an electron energy loss

(EEL) spectrum image of 256 × 256 pixels may be acquired in about 1 min.[18] At least low-loss EEL spectrum images (up to ∼50 eV energy losses) are effectively acquired at this rate, with sufficient signal-to-noise ratio to allow for successful mapping of this regime.

In this study we evaluate the impact of strain on the low-loss EELS properties. To do this we investigate the bulk plasmon energy for a series of AlN samples which all have unique strain states as measured by XRD reciprocal space mapping. To corroborate our experimental findings, full potential calculations of the AlN energy loss functions at different strain states was employed and was further extended to the group-III nitrides gallium nitride (GaN) and indium nitride (InN). Finally, a strategy for separating strain and composition effects in a low-loss measurement is discussed.

II. EXPERIMENTAL DETAILS

Three different sample types were grown by ultrahigh-vacuum magnetron sputter epitaxy (MSE).[19] Two of the samples are multilayer $Al_{1-x}In_xN$ samples (ML) of different composition grown on ZnO (0001) (ML-ZnO) and Al_2O_3 (0001) (ML-Al_2O_3) substrates, respectively. The ML samples consist of six layers covering the full compositional range starting from a pure AlN layer and followed by additional $Al_{1-x}In_xN$ layers where the In content increases for each layer until a pure InN layer is accomplished. The composition of the layers was determined using RBS (not shown). The AlN layers were found to be stoichiometric without detectable levels of impurities (i.e., O). The ML-ZnO and ML-Al_2O_3 samples were both grown at room temperature. The third sample, a thick single-layer (SL) AlN, was grown on Al_2O_3 (0001) (SL-Al_2O_3) substrate at 1000 °C as a reference sample.

Specimens for cross-sectional TEM analysis were prepared using mechanical polishing followed by Ar^+ ion milling at 5 keV with a final step to reduce surface damage at 2 keV. All STEM-EELS analyses were performed using a Tecnai G^2 TF 20 UT STEM employing a Gatan ENFINA parallel EEL spectrometer. The low-loss spectra were recorded in image-coupled mode using a <1 nm electron probe, with convergence angle ∼10 mrad and acceptance angle 1 mrad, energy dispersion 0.05 eV/channel, and 30 ms dwell time.

To enable plasmon peak position determination with high accuracy, 600 low-loss EEL spectra were binned and to exclude the effect of surface plasmons (from the upper and lower side of the TEM sample as well as from surface damage/surface relaxation), the measurements were done in such a thick region that we could not detect any shift of the low-loss spectrum as compared to a thin region. Low-loss EEL spectra for each AlN layer were obtained by initial zero loss peak fitting, followed by Fourier-log deconvolution for plural scattering removal.[20] Finally, considering a single Gaussian function of the low-loss spectrum,[21] the EELS spectrum was fitted by a nonlinear least-squares (NLLS) curve-fitting method in a 2 eV window centered around the most intense part of the plasmon peak for extracting bulk plasmon energy with fitting accuracy of 0.01 eV.

For high intensity and resolution reciprocal space mapping (RSM), over 0002 and $10\bar{1}5$ reciprocal lattice points, the beam of pure Cu Kα1 radiation, produced through a parabolically curved graded multilayer mirror followed by a two-bounce symmetric channel-cut Ge(220) monochromator, was used as the primary optics. A 1° receiving slit as analyzer was used for RSM to collect the diffracted beam.

The elemental compositions of the three samples were determined by RBS, where 2 MeV $^4He^+$ ions were used at an incident angle of 7° off from the surface normal to avoid channeling effects in the crystalline structure. The back scattered $^4He^+$ ions were detected at a scattering angle of 172° and the experimental data was simulated by the SINMAR 6.05 software.[22]

III. CALCULATION DETAILS

Calculations were done employing the full potential linearized augmented plane-wave program WIEN2K[23] in the generalized gradient approximation (GGA). Published experimental values for the lattice parameters were used as input for the calculations of AlN, InN, and GaN.[24,25] The muffin-tin radii for the elements were 1.66, 1.77, and 1.95 atomic units (a.u.) for Al, Ga, and In, respectively, with corresponding R_MT for the N atom. The maximum angular momentum l_{max} for the radial wave functions was set to 10 and the cutoff of the plane-wave expansion $R_{MT} \times K_{max}$ was 7. After a self-consistency cycle was performed with a total of 10 000 k points, these were increased to a total of 100 000 k points (4800 irreducible for AlN, GaN, and InN), which was necessary to calculate the optical properties. Eigenvalues up to 5.5 Ry above the Fermi level were calculated.

The optical properties were calculated using the OPTIC subroutine of WIEN2K, which yields the dielectric function from which the energy-loss function is obtained.[26] Since the Wurtzite structure of the III nitrides is anisotropic, the dielectric function is described by a tensor.[27] Because of this, two components (xx and zz) are calculated simultaneously. For this investigation, primarily the xx component is of interest as it is excited by the electron beam in the cross-sectional sample.

For most calculations of the loss function, a Gaussian broadening of only 0.1 eV was applied to achieve a high level of detail in the energy-loss spectra. This primarily emphasizes the interband transitions. When finally comparing the calculated and experimental spectra, a broadening of 1.0 eV was employed to reflect the energy resolution of our STEM at the applied experimental conditions.

IV. RESULTS

Cross-sectional STEM images of the investigated samples viewed along the $[11\bar{2}0]$ zone axis for $Al_{1-x}In_xN$ are shown in Fig. 1. The multilayer (ML) samples, ML-ZnO and ML-Al_2O_3, have a similar crystal-structure quality of their respective layers. Each ML sample contains six layers starting with AlN (closest to the substrate), followed by ternary alloys of $Al_{1-x}In_xN$ and finally InN at the top. As can be seen, the ML samples exhibit relatively smooth interfaces (indicated by arrows) between layers and surface. The total thickness of ML-ZnO and ML-Al_2O_3 samples is ∼400 nm. The AlN layer in the ML-ZnO sample is ∼70 nm thick and is referred to as "AlN+," while the AlN layer in the ML-ZnO sample is ∼40 nm thick and denoted "AlN–." The STEM image reveals

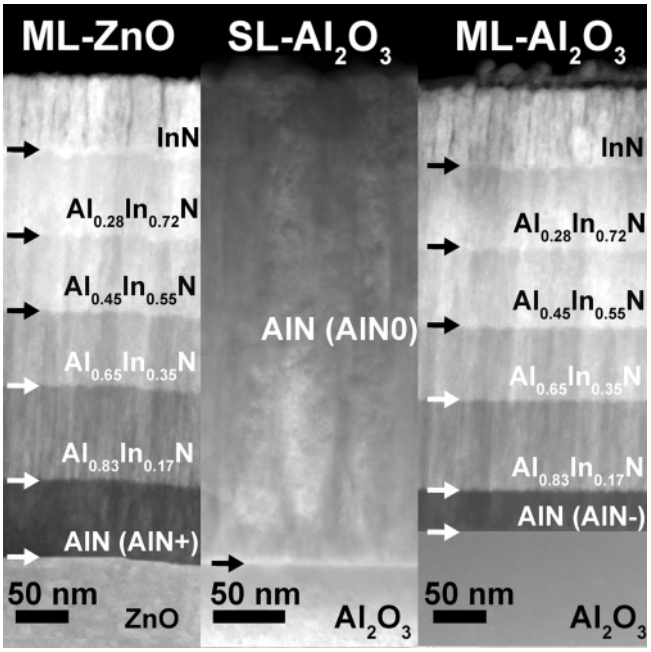

FIG. 1. Cross-sectional STEM images from three different samples: ML-ZnO, SL-Al_2O_3, and ML-Al_2O_3. Interfaces between different layers are indicated by arrows. Differently strained AlN layers are also indicated as AlN+, AlN0, and AlN–.

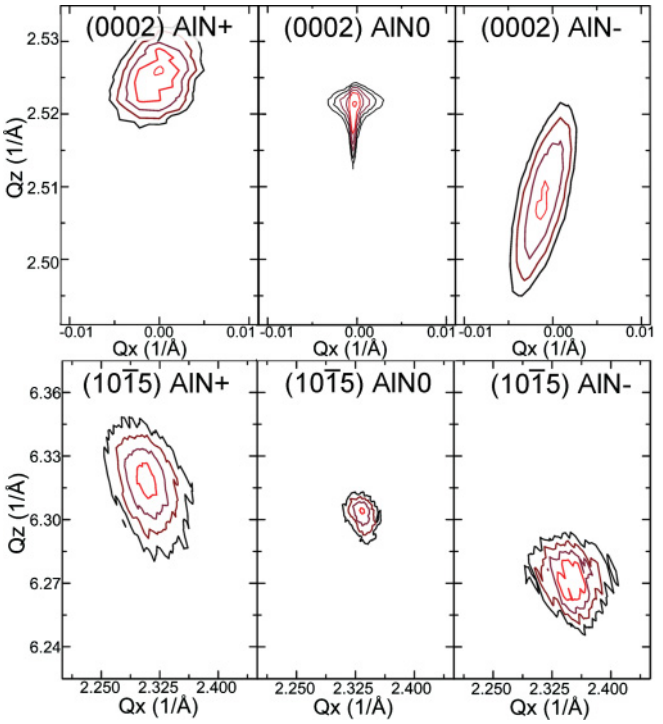

FIG. 2. (Color online) RSMs of AlN layers. Top: symmetric 0002 reflections; Bottom: asymmetric 10$\bar{1}$5 reflections (log scale is used for the contour plot).

that the single-layer AlN sample is ∼450 nm thick, exhibits a smooth surface, and contains some threading defects. This thick AlN layer is used as a reference and is denoted "AlN0."

Figure 2 shows RSMs of the AlN layers, AlN+, AlN0, and AlN–, around the symmetric 0002 and asymmetric 10$\bar{1}$5 reflections. Apparently, the AlN+ and AlN− sample contours of both the 0002 and 10$\bar{1}$5 reflections reveal opposite shifting with respect to the AlN0 sample. Through extracting the a and c lattice parameters from these maps, shown in Table I, the unit-cell volume and strain state of the AlN layers was determined. Only AlN0 has the same lattice parameters as reported for strain-free bulk AlN.[24] The AlN+ and AlN− exhibit biaxial tensile and compressive lateral strain, respectively. The unit-cell volume difference (ΔV) of the AlN layer compared to bulk values is calculated, resulting in ΔV values for the samples AlN+, AlN0, and AlN− of +1.85, 0, and −0.85%, respectively, giving a 2.7% volume difference between AlN+ and AlN− lattice crystals. The obtained structural details are summarized in Table I.

The measured low-loss EEL spectra from the different AlN layers are presented in Fig. 3 at (a) low dispersion and (b) high dispersion. The spectra contain a single peak each, which is attributed to the bulk plasmon loss of the AlN layers. As can be seen, the energy-loss spectrum is shifted between the differently strained AlN layers. The energy loss of the AlN0 bulk plasmon peak is situated at 20.46 eV (±0.01 eV). The tensile strained AlN+ resulted in a red shift of the bulk plasmon peak position, while the compressively strained AlN− is blue shifted, such that for AlN+ and AlN− the peak positions are located at 20.29 and 20.71 eV, respectively. The difference in strain state and hence volume between AlN+ and AlN− thus yields a total experimental bulk plasmon peak position difference of 0.42 eV. For the total volume difference of 2.7% between AlN+ and AlN−, this indicates that a 1% unit-cell volume change results in a 0.156 eV bulk plasmon peak position change, assuming a linear change of the bulk plasmon energy with volume. While plotting the spectra of Fig. 3, the total intensity of the spectra were first normalized and then shifted from the reference spectrum (AlN0) by a factor relative to the experimentally obtained volume change, e.g., AlN+ is shifted a factor 1.85 upward and AlN− is shifted 0.85 downward. A straight line fit between the absolute peak positions, as shown in Fig. 3(b), indicates a linear shift of the peak, depending on the volume change. It should be noted, however, that the changes in volume due to strain are small, although significant, but may deviate from a linear appearance when more strain is applied, or from a more

TABLE I. Summary of experimental results.

Layer name	Substrate	Thickness, nm	a, Å	Δa, %	c, Å	Δc, %	ΔV, %	E_p, eV
AlN+	ZnO	70	3.144	+1.09	4.963	−0.34	+1.85	20.29
AlN0	Al_2O_3	450	3.11	0	4.98	0	0	20.46
AlN–	Al_2O_3	40	3.087	−0.74	5.009	+0.58	−0.85	20.71

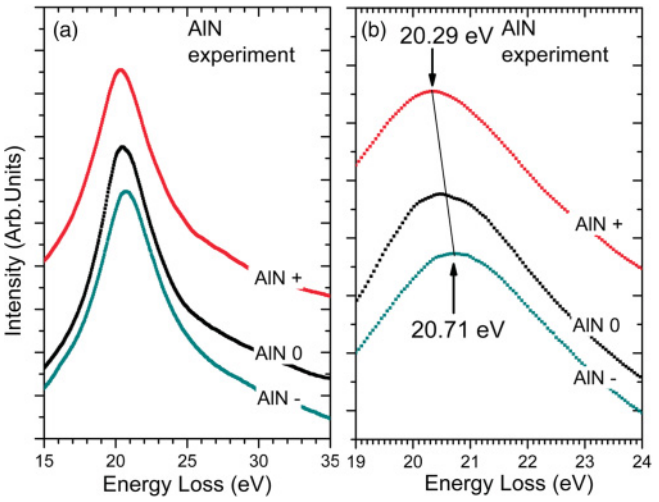

FIG. 3. (Color online) Deconvoluted low-loss EELS spectra from the three differently strained AlN layers at low dispersion (a) and high dispersion (b).

accurate measurement of the peak position. The results from the low-loss EELS measurement are summarized in Table I.

Figures 4 and 5 present the results from full potential calculations of the optical properties of AlN, revealing the impact of the lattice parameters on the energy-loss function. Only the interval of the energy-loss function where the main peak is located is shown. Figure 4 shows the simulated energy-loss spectra for when the AlN unit-cell volume is kept constant while inversely scaling a and c, i.e., by applying an isochoric strain to the unit cell, where the constant volume was calculated from the relaxed AlN lattice parameters. The change in the c parameter is indicated in the figure, ranging from -1% to $+1\%$. Figure 4 suggests that the appearance of the energy-loss function is not significantly affected by this type of lattice disturbance, although fine differences may be found. Considering that these calculations were carried out using only a 0.1 eV Gaussian broadening routine, these differences are, however, challenging to detect experimentally, even if a monochromated TEM was used. The simulated low-loss function of AlN, as the unit-cell volume is linearly varied from -3% to $+3\%$, while simultaneously keeping the c/a ratio constant (both a and c change by $+/-1\%$) is shown in Fig. 5. Here the ratio was obtained from the relaxed AlN lattice parameters. This nonisochoric strain results in a continuous shift of the bulk plasmon peak as well as the interband transitions. Following, for reference, one of the fine peaks on the central bulk plasmon peak of the function [Figs. 5(a) and 5(b)], one finds that in concert with the volume change, the peak shift is also linear, which is also seen for the spectra in Figs. 5(c) and 5(d), in which the broadened (by 1 eV) versions of the relaxed and $+/-3\%$ volume increase-strained unit cells are plotted.

V. DISCUSSION

The investigated AlN layers are found to be in relaxed and oppositely strained states due to different growth conditions with substrate type and growth temperature as well as layer thickness. AlN grown on the different substrates experiences a

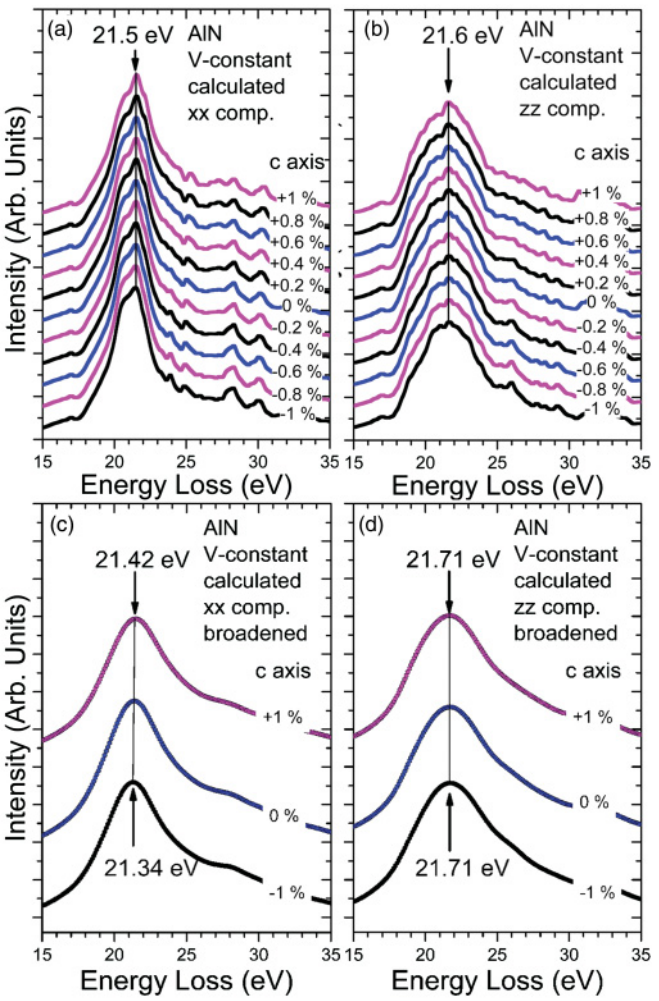

FIG. 4. (Color online) Simulated low-loss EELS spectra of AlN as a function of strain for constant cell volume, xx component (a) and zz component (b) and broadened spectra for xx component (c) and zz component (d).

lattice mismatch, which for AlN on ZnO and Al_2O_3 is -4.3% and $+13.3\%$, respectively. As a result, residual biaxial tensile and compressive strains are present in the films that are under non- or incomplete relaxation, as was shown by RSM. A partial strain relaxation over thickness can be observed in the 0002 reflection of the AlN0 map (see Fig. 2), where the reflection shows asymmetric contours. The smallest transverse scattering vector (**Qz**) value of the contour tail is very close to that of the thin AlN layer in the AlN− contour. This tail is attributed to the evolution of strain relaxation from the interface toward the film surface. Details about strain formation in the $Al_{1-x}In_xN$ layers can be found elsewhere.[19]

The low-loss spectra in Fig. 3 contain only one strong signal that is attributed to the bulk plasmon, which is a collective oscillation of the valence electrons. In the free electron theory, the valence electrons give a bulk plasmon energy according to

$$E_p = \hbar\omega_p = \hbar\left(\frac{ne^2}{\varepsilon_0 m_0}\right)^{1/2}, \quad (1)$$

where n is the density of electrons, e is the electron charge, ε_0 is the permittivity of free space, and m_0 is the electron mass.

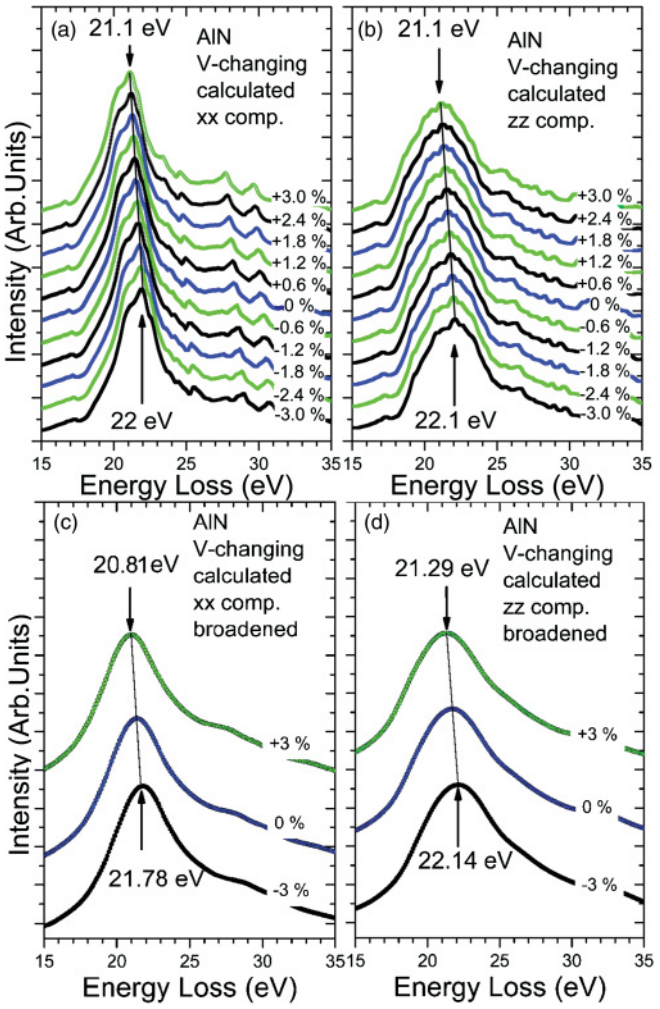

FIG. 5. (Color online) Simulated low-loss EELS spectrum of AlN by changing unit-cell volume (–3% to +3%) and keeping the *c/a* ratio constant, xx component (a) and zz component (b) and broadened spectra for xx component (c) and zz component (d).

This model gives a good approximation to the measured bulk plasmon energy, particularly for metallic systems.[15] However, it does not take into account damping of the bulk plasmon, which broadens the peak, and intraband transitions, which adds fine structure to the low-loss spectrum.

To resolve this shortcoming, we consider the fast electron passing through the sample as a time-varying electric field. The induced electric field in the material as a response to the electron is then given by the dielectric function in the small-angle region $\varepsilon(E) = \varepsilon_1(E) + i\varepsilon_2(E)$. Furthermore, the single scattering distribution may be written in the form[15,18,23]

$$S(E) = \frac{2I_0 t}{\pi a_0 m_0 v^2} \mathrm{Im}\left(\frac{-1}{\varepsilon(E)}\right) \ln\left[1 + \left(\frac{\beta}{\theta_E}\right)^2\right], \qquad (2)$$

where I_0 is the incident intensity, t the specimen thickness, v the speed of the incident electrons, β is the collection semiangle, and $\theta_E = E/(\gamma m_0 v^2)$ is the characteristic scattering angle (where $\gamma = 1 - v^2/c^2$), and ignoring the need for correction factors due to the high convergence/collection angle ratio. Thus the scattering distribution is proportional to Im[$-1/\varepsilon(E)$], where

$$\mathrm{Im}\left(\frac{-1}{\varepsilon(E)}\right) = \frac{\varepsilon_2(E)}{\varepsilon_1^2(E) + \varepsilon_2^2(E)} \qquad (3)$$

is known as the loss function. In principle, at large energy losses, $\varepsilon_1(E)$ approaches 1 while $\varepsilon_2(E)$ is small,[12] such that the energy-loss function is reduced to S(E) $\approx \varepsilon_2(E)$, although in most cases $\varepsilon_1(E)$ cannot be ignored. However, it is desirable to calculate $\varepsilon_2(E)$, since from this point it is possible to use Kramers-Kronig analysis to retrieve $\varepsilon_1(E)$. In the WIEN2K calculations applied here, $\varepsilon_2(E)$ is obtained from the random phase approximation (RPA),[20] which employs wave functions of the core and valence states, which are initially calculated by WIEN2K. Employing WIEN2K, it may be found that the real part $\varepsilon_1(E)$ of the dielectric function gives the bulk plasmon while the imaginary part $\varepsilon_2(E)$ gives the intraband transitions of the energy loss function as it was calculated in this paper. By comparing with the calculated real and imaginary parts of the dielectric function (not shown), the strong and slowly varying peaks throughout these calculations are attributed to bulk plasmons, while the finer structure is attributed to intraband transitions.

In these simulations a seemingly linear variation of the plasmon peak position is identified when the crystal volume is changed (Fig. 5). However, the peak position is not changed while changing the *c/a* ratio and keeping the volume constant (Fig. 4). The electron density is changed while calculating the loss functions for the different crystal volumes in Fig. 5. For a quick indication, Eq. (1) shows that the plasmon energy is proportional to electron density$^{\frac{1}{2}}$, indicating a nonlinear relation between the two. However, for such small changes as are observed here, the nonlinear behavior may appear as a seemingly linear variation.

To test the reliability of these calculations, the experimentally obtained lattice parameters for AlN+, AlN0, and AlN− were used as input. The resulting calculated energy-loss functions are shown in Fig. 6 for Gaussian broadenings of 0.1 and 1 eV. As with the experimental spectra, the intensity is

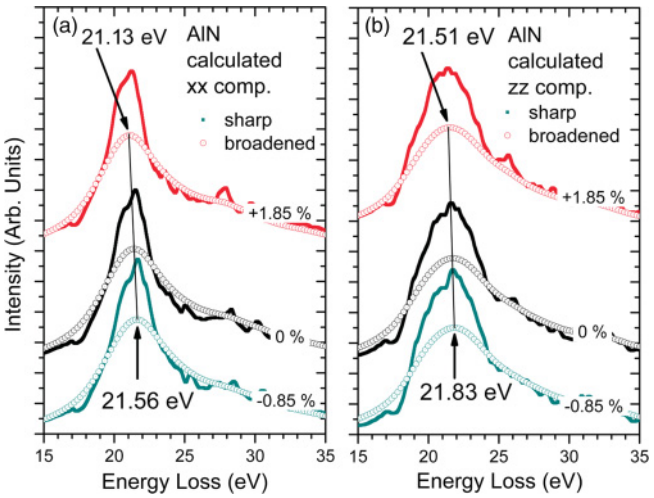

FIG. 6. (Color online) Simulated low-loss EELS spectrum of AlN by using experimentally determined lattice parameters, xx component (a) and zz component (b).

TABLE II. Comparison of simulated (using experimental lattice constants) and experimental plasmon peak position values for differently strained AlN layers.

Layer name	Calculated AlN (xx), eV	Rel. Cal. AlN (xx), eV	Expt. AlN E_p, eV	Rel. Expt. AlN, eV
AlN+	21.13	−0.24	20.29	−0.17
AlN0	21.37	0	20.46	0
AlN–	21.56	+0.19	20.71	+0.25

normalized and shifted from the unstrained sample by a factor corresponding to the volume change. Also, here it is found that the plasmon is shifted linearly depending on volume, although the *c/a* ratio is not the same for either the AlN+, AlN0, or AlN–, which was the case in Fig. 5. This suggests that the plasmon peak position shift is more depending on the associated volume change than differences in a or c individually. This also indicates that the strain in both a and c cannot be obtained separately from a measurement of the bulk plasmon peak energy alone. Although the simulated peak positions do not perfectly fit the experimental ones (they are shifted by 1.1 eV), their relative peak shift matches. The AlN+ peak is found with a maximum at 21.11 eV, the unstrained AlN0 at 21.37 eV, and finally for the AlN–, the peak energy was 21.56 eV. The total energy difference between AlN+ and AlN− was 0.44 eV. This gives a calculated shift of 0.159 eV per 1% volume change as compared to the experimentally measured shift of 0.156 eV. A comparison of simulated (using experimental lattice constants) and experimental bulk plasmon peak position values for the differently strained AlN layers is given in Table II.

Similar calculations were applied to GaN and InN, where the plasmon peak energy is located at 19.4 eV for GaN[28] and 14.95 eV for InN as determined experimentally,[16] and the results are shown for the relaxed and +/−3% volume unit cells in Fig. 7. Here, the energy-loss function is more complex with significantly stronger intraband contributions. However, by following the bulk plasmon shift for the broadened spectrum for each structure, as is indicted in Fig. 7, the relative energy shifts per 1% volume change are 0.168 eV for GaN and 0.079 eV for InN. These numbers are of a similar order as for AlN. The simulation results are summarized in Table III.

By alloying these nitrides, we recently found that the plasmon peak changes linearly in the interval between the pure components.[16] We suggest here that a ternary nitride alloy, which is subject to strain, experiences a similar shift of the plasmon peak position away from the relaxed value, as for the binary nitrides discussed above.

Without prior knowledge of the exact composition of an alloy, it is possible to determine this by determining the bulk plasmon peak position. However, employing this method assumes a relaxed structure, so the composition of a crystal might be over- or underestimated because of the strain-induced shifts the bulk plasmon energy. For $Al_{1-x}In_xN$ alloys, where the plasmon ranges from 14.95 to 20.4 eV,[16] the compositional error is only ∼3% for a 1% increase in volume in Al-rich $Al_{1-x}In_xN$ and ∼9% for a 1% increase in both a and c lattice

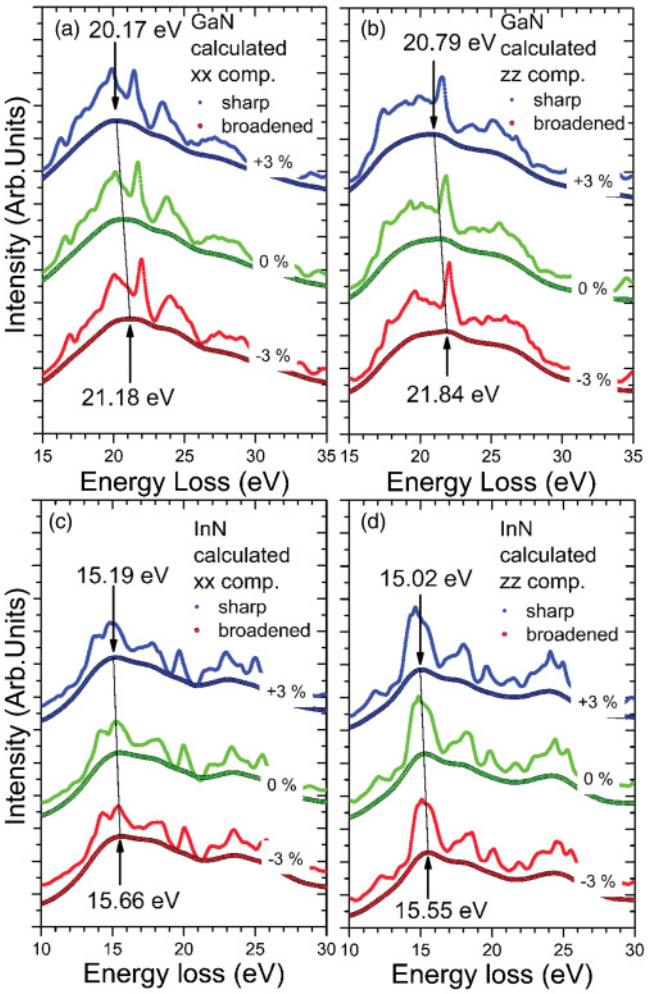

FIG. 7. (Color online) Simulated low-loss EELS spectrum of InN and GaN by changing the unit-cell volume from −3% to +3% and keeping the c/a ratio constant for the components (a) GaN xx, (b) GaN zz, (c) InN xx, and (d) zz.

parameters (3% change in volume). On the other hand, for $Al_{1-x}Ga_xN$ where the plasmon energy range is only 1 eV, the compositional error is ∼16% for a 1% change in volume and an alarming ∼48% for a 1% increase in both a and c lattice parameters (3% change in volume).

Applying spectrum imaging methods to nanoscale structures such as quantum wells and ignoring for the purpose of this discussion the delocalization effect of the low-loss features,[29] the map or line scan along the nanostructure will show a variation in the plasmon energy across the interface due to variations in composition. Since the two materials on either side of the interface are usually not perfectly lattice matched, at least the quantum material will experience strain, affecting plasmon peak position as well. The plasmon energy of the quantum structure cannot directly reveal the composition. However, if a and c are known from, e.g., a lattice image, the crystal volume is known. Then the bulk plasmon position can be used to determine the composition and the strain of the lattice.

TABLE III. Calculated bulk plasmon peak position values for InN, GaN, and AlN (xx and zz components).

ΔV, %	InN (xx), eV	InN (zz), eV	GaN (xx), eV	GaN (zz), eV	AlN (xx), eV	AlN (zz), eV
+3%	15.19	15.02	20.17	20.79	20.81	21.29
0	15.43	15.29	20.68	21.32	21.37	21.73
−3%	15.66	15.55	21.18	21.84	21.78	22.14

VI. CONCLUSIONS

The low-loss EELS spectrum is affected by the strain state in group-III nitrides, which was shown by a combination of experimental and theoretical experiments. It is found that the bulk plasmon peak position varies nearly linearly with the unit-cell volume, at least up to a 3% volume change This can be used to retrieve information about the strain in the material. Specifically, a volume change of 1% results in a peak shift of 0.159, 0.168, and 0.079 eV for AlN, GaN, and InN, respectively. The AlN peak shift was confirmed experimentally with a measured peak shift of 0.156 eV per 1% volume change. This result has particular relevance for low-loss mapping studies of confined and nanoscale structures in alloys of group-III nitrides. As strain and compositional gradients are typically present across the interfaces of these, it is difficult to discern which of these causes a shift in the low-loss spectrum. It is further concluded that strain has a lower impact on the peak shift in $Al_{1-x}In_xN$ and $In_{1-x}Ga_xN$ alloys than for $Al_{1-x}Ga_xN$. For example, a 1% volume change in $Al_{1-x}In_xN$ causes a detectable peak shift, which could be misinterpreted for a 3% compositional variation of Al and In. With a similar peak shift, for $Al_{1-x}Ga_xN$, the 1% volume change may be misinterpreted for an ∼16% composition change. As strain between layers of widely differing composition that are a few monolayers thick can be larger than this, low-loss studies must be undertaken with a full knowledge of both the strain state and the composition of the material. Identification of the two components can be obtained by real or reciprocal space measurements for the lattice spacing combined with low-loss EELS.

ACKNOWLEDGMENTS

This work was supported by the Swedish Research Council (VR), the Swedish Foundation for Strategic Research (SSF), and The Royal Swedish Academy of Sciences (KVA).

*juspa@ifm.liu.se

[1] J. Wu, J. Appl. Phys. **106**, 011101 (2009).
[2] M. Razeghi and R. McClintock, J. Cryst. Growth **311**, 3067 (2009).
[3] M. Chu, Y. Sun, U. Aghoram, and S. E. Thompson, Annu. Rev. Mater. Res. **39**, 203 (2009).
[4] W. Zhao, G. Duscher, G. Rozgonyi, M. A. Zikry, S. Chopra, and M. C. Ozturk, Appl. Phys. Lett. **90**, 191907 (2007).
[5] V. Darakchieva, M. Beckers, M. Xie, L. Hultman, B. Monemar, J. Carlin, E. Feltin, M. Gonschorek, and N. Grandjean, J. Appl. Phys. **103**, 103513 (2008).
[6] J. Chung, G. Lian, and L. Rabenberg, Appl. Phys. Lett. **93**, 081909 (2008).
[7] P. L. Galindo, S. Kret, A. M. Sanchez, J. Laval, A. Yanez, J. Pizarro, E. Guerrero, T. Ben, and S. I. Molina, Ultramicroscopy **107**, 1186 (2007).
[8] P. Zhang, A. A. Istratov, E. R. Weber, C. Kisielowski, H. He, C. Nelson, and J. C. H. Spence, Appl. Phys. Lett. **89**, 161907 (2006).
[9] A. Beche, J. L. Rouviere, L. Clement, and J. M. Hartmann, Appl. Phys. Lett. **95**, 123114 (2009).
[10] M. Hytch, F. Houdellier, F. Hue, and E. Snoeck, Nature **453**, 1086 (2008).
[11] F. Houdellier, M. J. Hÿtch, E. Snoeck, and M. J. Casanove, Mater. Sci. Eng. B **135**, 188 (2006).
[12] R. F. Egerton, *Electron Energy loss Spectroscopy in the Electron Microscope* (Plenum, New York, 1996).
[13] H. Raether, *Excitations of Plasmons and Interband Transitions by Electrons* (Springer, Berlin, 1980).
[14] V. J. Keast, J. Electron Spectrosc. **143**, 97 (2005).
[15] A. M. Sanchez, R. Beanland, M. H. Gass, A. J. Papworth, P. J. Goodhew, and M. Hopkinson, Phys. Rev. B **72**, 075339 (2005).
[16] J. Palisaitis, C.-L. Hsiao, M. Junaid, M. Xie, V. Darakchieva, J. Carlin, N. Grandjean, J. Birch, L. Hultman, and P. O. Å. Persson, Phys. Status Solidi (RRL) **5**, 50 (2011).
[17] N. D. Browning, I. Arslan, R. Erni, J. C. Idrobo, A. Ziegler, J. Bradley, Z. Dai, E. A. Stach, and A. Bleloch, J. Phys. Conf. Ser. **26**, 59 (2006).
[18] A. Gubbens, M. Barfels, C. Trevor, R. Twesten, P. Mooney, P. Thomas, N. Menon, B. Kraus, C. Mao, and B. McGinn, Ultramicroscopy **110**, 962 (2010).
[19] C.-L. Hsiao, J. Palisaitis, M. Junaid, P. O. Å. Persson, J. Jensen, and J. Birch, Thin Solid Films (submitted).
[20] R. F. Egerton, Micron **34**, 127 (2003).
[21] A. Maigne and R. D. Twesten, J. Electron Microsc. **58**, 99 (2009); [http://www.rzg.mpg.de/∼mam].
[22] K. Schwarz and P. Blaha, Comput. Mater. Sci. **28**, 259 (2003).
[23] H. Morkoc, *Nitride Semiconductors and Devices* (Springer-Verlag, Germany, 1999).
[24] T. Yao and S. K. Hong, *Oxide and Nitride Semiconductors: Processing, Properties, and Applications* (Springer-Verlag, Germany, 2009).
[25] C. Ambrosch-Draxl and J. O. Sofo, Comput. Phys. Commun. **175**, 1 (2006).
[26] C. Ambrosch-Draxl, J. A. Majewski, P. Vogl, and G. Leising, Phys. Rev. B **51**, 9668 (1995).
[27] P. Schattschneider, Ultramicroscopy **28**, 1 (1989).
[28] V. J. Keast, A. J. Scott, M. J. Kappers, C. T. Foxon, and C. J. Humphreys, Phys. Rev. B **66**, 125319 (2002).
[29] D. A. Muller and J. Silcox, Ultramicroscopy **59**, 195 (1995).